Research Article | Vol. 9, No. 10 | 1 Oct 2018 | BIOMEDICAL OPTICS EXPRESS 4689
Biomedical Optics EXPRESS

High-speed widefield photoacoustic microscopy of small-animal hemodynamics

Bangxin Lan,[1,6] Wei Liu,[1,6] Ya-chao Wang,[2] Junhui Shi,[3] Yang Li,[4] Song Xu,[5] Huaxin Sheng,[2] Qifa Zhou,[4] Jun Zou,[5] Ulrike Hoffmann,[2] Wei Yang,[2] and Junjie Yao[1,*]

[1]*Department of Biomedical Engineering, Duke University, Durham, NC 27708, USA*
[2]*Center for Perioperative Organ Protection (CPOP), Department of Anesthesiology, Duke University Medical Center, Durham, NC 27710, USA*
[3]*Caltech Optical Imaging Laboratory, Andrew and Peggy Cherng Department of Medical Engineering, Department of Electrical Engineering, California Institute of Technology, Pasadena, CA 91125, USA*
[4]*Department of Biomedical Engineering, University of Southern California, Los Angeles, CA 90089, USA*
[5]*Department of Electrical and Computer Engineering, Texas A&M University, College Station, Tx 77843, USA*
[6]*These authors contributed equally as first author.*
[*]*junjie.yao@duke.edu*

Abstract: Optical-resolution photoacoustic microscopy (OR-PAM) has become a popular tool in small-animal hemodynamic studies. However, previous OR-PAM techniques variously lacked a high imaging speed and/or a large field of view, impeding the study of highly dynamic physiologic and pathophysiologic processes over a large region of interest. Here we report a high-speed OR-PAM system with an ultra-wide field of view, enabled by an innovative water-immersible hexagon-mirror scanner. By driving the hexagon-mirror scanner with a high-precision DC motor, the new OR-PAM has achieved a cross-sectional frame rate of 900 Hz over a 12-mm scanning range, which is 3900 times faster than our previous motor-scanner-based system and 10 times faster than the MEMS-scanner-based system. Using this hexagon-scanner-based OR-PAM system, we have imaged epinephrine-induced vasoconstriction in the whole mouse ear and vascular reperfusion after ischemic stroke in the mouse cortex *in vivo*, with a high spatial resolution and high volumetric imaging speed. We expect that the hexagon-scanner-based OR-PAM system will become a powerful tool for small animal imaging where the hemodynamic responses over a large field of view are of interest.

1. Introduction

Optical-resolution photoacoustic microscopy (OR-PAM) has been playing an increasingly important role in small animal studies [1], taking advantage of its rich optical absorption contrast [2], high spatial resolution [3], and intrinsic volumetric imaging capability [4]. The traditional OR-PAM systems usually employ a confocal and coaxial configuration of the optical excitation beam and acoustic detection beam, maximizing the detection sensitivity and optimizing the spatial resolutions [5–7]. Volumetric imaging is typically achieved by point-by-point raster scanning of the optical and acoustic beams using stepper motor scanning stages [8–18]. Because of the fine scanning step size required by the micron-level lateral resolution [8], the scanning speed of OR-PAM is traditionally low (about 1-Hz B-scan rate over a 1-mm scanning range) [19, 20]. Such a low imaging speed has long prevented OR-PAM from obtaining tissue's dynamic information, such as transient drug responses and brain functions.

Many efforts have been attempted to speed up OR-PAM, which can be grouped into two major categories: (1) fast mechanical scanning of both optical and acoustic beams, and (2)

#340439 https://doi.org/10.1364/BOE.9.004689
Journal © 2018 Received 25 Jul 2018; revised 3 Sep 2018; accepted 4 Sep 2018; published 7 Sep 2018

Biomedical Optics EXPRESS

fast optical scanning of the optical beam only [21]. While mechanical scanning is more convenient to maintain the confocal and coaxial alignment of the optical and acoustic beams over a large scanning range, optical scanning can achieve a much higher scanning speed over a small scanning range. To improve the mechanical scanning speed, Ma *et al*. used a piezo linear translation stage, providing a B-scan rate of ~9 Hz over a 1-mm scanning range [5]; Wang *et al*. employed a voice-coil linear translation stage to improve the B-scan rate to 40 Hz over a 1-mm scanning range [22]. Compared to mechanical scanning, optical scanning can further improve the imaging speed by at least 10 times [23–25]. Xie *et al*. were the first to use a two-dimensional (2D) Galvo scanning mirror with a flat ultrasonic transducer, providing a B-scan rate of 17 Hz over a 6-mm scanning range [25]. Later, Rao *et al*. used the same scanning approach with a focused ultrasonic transducer, and achieved a B-scan rate of 60 Hz over a 0.3-mm scanning range [24]. The high-speed scanning of only the optical beam leads to a relatively low signal-to-noise ratio (SNR) and scanning range, limited by either the unfocused ultrasound detection or the small acoustic focal area. Several hybrid-scanning approaches combining 1D optical scanning and 1D mechanical scanning were reported with concurrent scanning of focused optical and acoustic beams [26, 27]. Kim *et al*. used a 1D Galvo-mirror immersed in non-conducting liquid hydrofluoroether, providing a B-scan rate of 60 Hz over a 4-mm scanning range [26]. However, the low acoustic impedance of hydrofluoroether resulted in significant PA signal attenuation. Xi *et al*. recently employed a rotatory scanning of cylindrically focused ultrasound detection to enlarge the field of view, which, however, has inferior detection sensitivity than the spherically focused ultrasound detection [28, 29]. We previously developed high-speed OR-PAM using a customized 1D water-immersible MEMS scanning mirror [30], with a B-scan rate of 400 Hz over a 3-mm scanning range. However, when the MEMS mirror is not driven at its resonant frequency, the scanning range is substantially reduced to less than 1 mm. The limited scanning range of the MEMS mirror prevents OR-PAM imaging a large field of view, such as the entire mouse brain cortex (~10 mm in length and width). Therefore, a novel scanning method is highly desired for OR-PAM that can simultaneously achieve (1) a high imaging speed for dynamic imaging, (2) a large scanning range for a wide field of view, and (3) confocal scanning of optical and acoustic beams for high detection sensitivity.

Here, we present a wide-field high-speed OR-PAM system based on a novel water-immersible hexagon-mirror scanner, or HM-OR-PAM. Using the hexagon scanning mirror steered by a water-immersible high-precision DC motor, HM-OR-PAM has achieved a maximum B-scan rate of 900 Hz over a 12-mm scanning range, while maintaining confocal alignment of the optical and acoustic beams. The volumetric imaging speed of the HM-OR-PAM over a 1 × 1 cm^2 region is 3900 times faster than that of the second-generation OR-PAM [31], 300 times faster than the voice-coil-based OR-PAM [22], and at least 10 times faster than our MEMS-based OR-PAM [30]. To demonstrate the dynamic imaging of biological activities *in vivo*, we monitored the epinephrine-induced vasoconstriction in the entire mouse ear, and the blood reperfusion after ischemic stroke in the entire mouse cortex. These results have collectively demonstrated the high-speed widefield imaging capability of HM-OR-PAM for preclinical applications.

2. Methods

2.1. The HM-OR-PAM system

Figure 1(a) shows the schematic of the HM-OR-PAM system. A pulsed Nd: YAG laser (VPFL-G-20, V-gen, Tel Aviv, Israel) is the optical excitation source with a wavelength of 532 nm and a pulse repetition rate of up to 800 kHz. The collimated laser light is focused by a plano-convex lens with a focal length of 75 mm (AC127-075-A, Thorlabs, Newton, USA), and directed by a right-angled prism through the center aperture of a focused ring-shaped ultrasonic transducer, and then steered by a lab-made hexagon-mirror scanner towards the sample surface. The resultant photoacoustic signals are reflected by the hexagon mirror and

Biomedical Optics EXPRESS

received by the ultrasonic transducer. The ultrasonic transducer has a central frequency of 40 MHz, a −6-dB bandwidth of 70%, and a focal length of 14 mm. The focused light beam is aligned coaxially and confocally with the ultrasonic transducer to maximize the detection sensitivity.

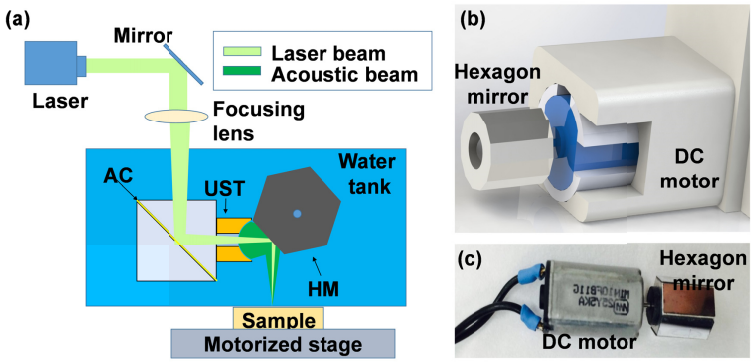

Fig. 1. Hexagon-mirror based optical-resolution photoacoustic microscopy (HM-OR-PAM). (a) Schematic of the HM-OR-PAM system. AC, aluminum coating; HM, hexagon mirror; UST, ultrasonic transducer. (b) 3D drawing and (c) photograph of the hexagon scanning mirror driven by a high-speed DC-motor.

We have developed the hexagon-mirror scanning system that can steer both light and sound beams under water, enabling high-speed imaging with a large field of view (Fig. 1(b); Visualization 1). The hexagon mirror was made of BK-7 glass and the six facets were coated with protective aluminum for wideband optical and acoustic reflection. The mirror has a diameter of 1 cm and a length of 8 mm. Each facet is 5 mm by 8 mm, which matches the ultrasonic transducer's detection aperture. To actuate the hexagon mirror, a water-immersible brushed micro-DC motor (A-max 12, Maxon Motor, Swiss) was co-axially assembled with the hexagon mirror's central aperture (Fig. 1(c)). By adjusting the amplitude of the driving voltage from 0.2 V to 5 V, the DC motor's revolution rate can be flexibly adjusted from 1 Hz to 150 Hz. Since each revolution of the DC motor provides six repeated cross-sectional scans (B-scan), the hexagon mirror scanner can achieve a B-scan rate of up to 900 Hz. \

For each laser pulse, one time-resolved A-line signal along the acoustic axis is reflected by the hexagon mirror and detected by the focused ultrasonic transducer. Because the speed of sound (1500 m/s in water) is much faster than the rotating speed of the hexagon mirror, the movement of the hexagon mirror during each A-line signal is negligible. The PA signal received by the ultrasonic transducer is amplified by 51 dB and sampled by a 12-bit DAQ card at 500 MHz (ATS9350, AlarzarTech, Pointe-Claire, QC, Canada). Volumetric imaging is achieved by the fast hexagon-mirror scanning along the x-axis and the slow stepper-motor scanning along the y-axis (PLS-85, Physik Instrumente, Karlsruhe, Germany). The laser firing, hexagon scanner rotating, stepper motor scanning, and the DAQ sampling are synchronized by an FPGA card (myRIO, National Instruments, Austin, TX, USA).

2.2. Scanning speed and scanning range

One major advantage of the hexagon-mirror scanner over our previous MEMS-mirror scanner is the consistent scanning range, regardless of the scanning speed (i.e., revolution rate of the DC motor). The measured revolution rate of the DC motor is proportional to the driving voltage, as shown in Fig. 2(a). The scanning range of the hexagon mirror is consistently 12 mm at all tested DC motor speeds. With a laser pulse repetition rate of 600 kHz, the revolution rate of the DC motor only affects the spatial sampling density between each A-line signal, *i.e.*, the effective scanning step size along the x-axis. The total data acquisition time of

Biomedical Optics EXPRESS

a volumetric image is determined by the slow motor scanning speed and range along the *y*-axis.

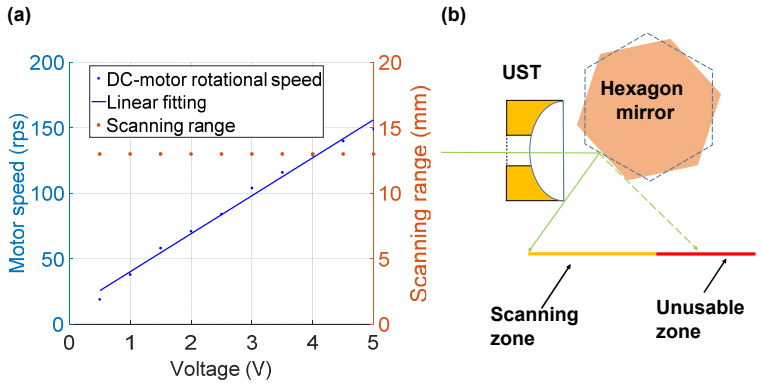

Fig. 2. The scanning characteristics of the hexagon-mirror scanner. (a) The revolution rate and the scanning range of the hexagon-mirror scanner as a function of the driving voltage applied to the DC motor. (b) Schematic of the usable scanning zone (yellow) and unusable zone outside the detection region of the ultrasonic transducer (red).

The 12-mm scanning range of the hexagon mirror scanner is jointly determined by the size of the hexagon (or the maximum scanning angle of each hexagon facet), the focal length and focal zone of the optical focusing lens, and the focal length of the ultrasonic transducer. Because of the continuous rotation of the hexagon mirror, about 60% of the laser pulses steered by each facet fall on the sample surface, while the remaining 40% laser pulses are directed either on the surface of the ultrasonic transducer or outside the detection zone, as shown in Fig. 2(b). When the laser beam is steered closer to the edges of each hexagon facet, the sample surface gradually falls out of the focal zone of the laser beam and the ultrasonic transducer, resulting in a low detection sensitivity. As the rotation of the hexagon mirror driven by the DC motor is independent of the laser firing, we use the strong PA signals generated by the ultrasonic transducer surface as the 'start-of-scan' markers to align each B-scan.

2.3. Spatial resolutions

During the rotational scanning of the hexagon mirror, the size of the laser spot on a flat sample surface depends on the scanning angle. Thus, the lateral resolution of the HM-OR-PAM system changes along the fast scanning *x*-axis. We quantified the lateral resolutions at different scanning angles (Fig. 3), by measuring the full width at half maximum (FWHM) of the corresponding line spread functions (LSF), which were derived from the edge spread functions of the USAF resolution target (58-198, Edmund Optics, Barrington, NJ, USA). The initial laser spot position (x = 0 mm) was defined as the position with a zero-degree beam angle.

Due to the geometrical divergence of the optical focusing over a flat sample surface, the lateral resolution within the scanning range changes from 8.8 µm (x = 0 mm) to 31.9 µm (x = 8 mm), as shown in Fig. 3(a). The maximum positive and negative scanning ranges are not the same because part of the negative scanning is blocked by the ultrasonic transducer, as shown in Fig. 2(b). Eventually, at the far ends beyond the scanning range, the optical path length changes quickly with the scanning angle, leading to a large increase in the laser spot size on the sample surface. Figure 3(b) shows the measured LSFs at a representative position of x = –4 mm, providing a lateral resolution of 10 µm. The theoretical lateral resolution is 8.2 µm at 532 nm with an effective optical NA of 0.033, which is close to the best lateral resolution measured at x = 0 mm. Unlike the lateral resolution, the axial resolution of the HM-OR-PAM system is determined only by the bandwidth of the ultrasonic transducer and the

Biomedical Optics EXPRESS

speed of sound in water [32], which is around 33 μm and is consistent across the scanning range. As the diameters of microvessels in small animal models generally fall in the range of 10–100 μm [33], HM-OR-PAM can still meet the need of high-resolution imaging.

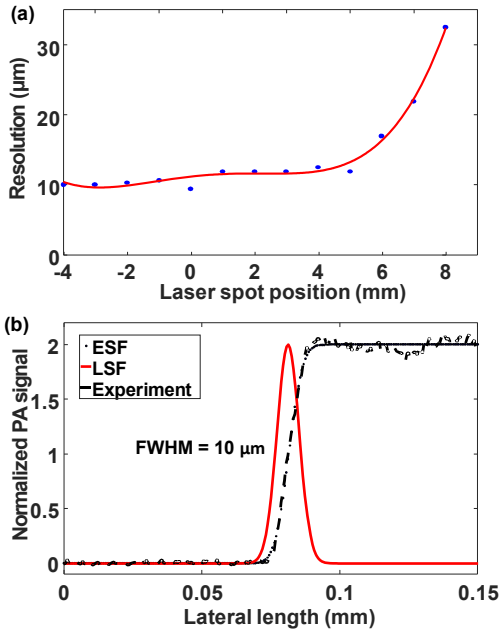

Fig. 3. The lateral resolution of HM-OR-PAM over the 12-mm scanning range. (a) Lateral resolution as a function of the laser spot position along the *x*-axis. (b) The measured FWHM of the LSF at a representative position of $x = -4$ mm.

2.4. Fast-scanning step size

The fast-scanning step size along the *x*-axis was jointly determined by revolution rate of the DC motor (or the B-scan rate), the scanning angle (or the lateral position of the laser spot), and the laser pulse repetition rate (PRR). The average scanning step size across the scanning range is proportional to the DC-motor rotational rate and inversely proportional to the laser PRR, as shown in Fig. 4(a). Thus, there is a tradeoff between the fast-scanning speed and the scanning step size. The PRR and DC-motor revolution rate can be readily adjusted to change the step size, according to the required imaging quality. Similar to the lateral resolution, for each B-scan with a fixed laser PRR, the step size of the hexagon scanning also changes over the 12-mm scanning range. Here, we only consider the variation of the scanning step size on a flat surface. The large scanning angle towards the ends of the scanning range leads to an increased step size. Figure 4(b) illustrates the gradual increase in the normalized step size with the scanning angle (or the lateral position of the laser spot), in which the step size is normalized by that at $x = 0$ mm. For instance, with a B-scan rate of 420 Hz and a laser PRR of 600 kHz, the scanning step size varies from 8.8 μm at $x = 0$ mm to 30 μm at $x = 8$ mm within the 12-mm scanning range. The computed scanning step sizes in Fig. 4(b) are in turn used for rescaling the acquired B-scan images. In practice, we also need to convert the rotational scanning coordinate into linear scanning coordinate, as detailed in our previous work [34], considering the scanning geometry and applying a 2D linear interpolation.

Biomedical Optics EXPRESS

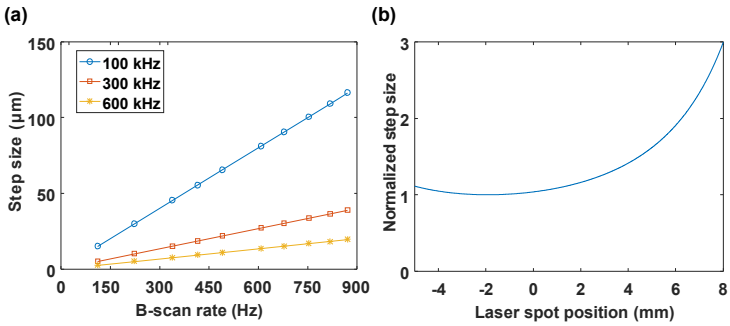

Fig. 4. The fast-scanning step size of the hexagon-mirror scanner. (a) Average fast-scanning step size over the 12-mm scanning range as a function of the laser PRR and B-scan rate. (b) The relative scanning step size normalized by that at $x = 0$.

3. Validating the system performance on phantoms and *in vivo*

To demonstrate the high-speed widefield imaging of the HM-OR-PAM system, a leaf phantom was imaged in clear medium with a B-scan rate of 420 Hz and 900 Hz, as shown in Fig. 5(a). All the following experiments were performed with a laser PRR of 600 kHz, unless otherwise noted. A leaf area of 20 × 12 mm^2 was imaged, and each volumetric imaging took 16 seconds. The PA signal strength within the 12-mm fast scanning range was approximately consistent, due to the relatively large depth of focus of the optical and acoustic beams. While the major branches of the leaf phantom were clearly resolved at both B-scan rates, the B-scan rate of 420 Hz expectedly resulted in better imaging quality due to the smaller fast-scanning step size, which is consistent with the estimation in Fig. 4.

In vivo imaging was performed on the ear of a female Swiss Webster mouse (10 weeks old and 25 grams in weight), with the protocol approved by the Institutional Animal Care and Use Committee (IACUC) of Duke University. All methods were performed in accordance with the relevant guidelines and regulations. The hair of the mouse ear was removed before imaging. During the imaging, the temperature of the mouse was held at 37 °C via a heating pad and the mouse was anesthetized via isoflurane (1.5% v/v). The laser PRR and the B-scan rate were the same as the above leaf phantom imaging. The imaging region of the entire mouse ear was 12 × 15 mm^2, and each volumetric imaging took 12 seconds. The *in vivo* images of the mouse ear vasculature were shown in Fig. 5(b), with a B-scan rate of 420 Hz and 900 Hz. Both images show microvasculature of the mouse ear. The image acquired at the B-scan rate of 420 Hz shows a higher resolution and more small vessels than that at the B-scan rate of 900 Hz.

Biomedical Optics EXPRESS

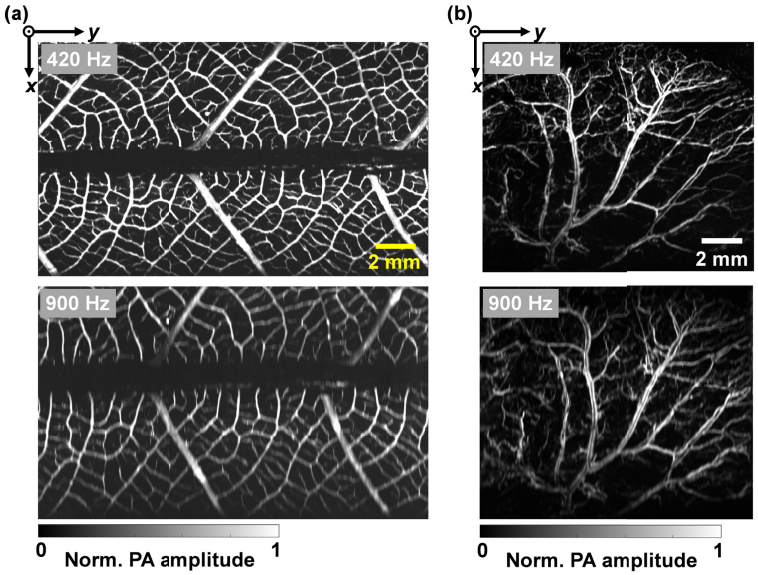

Fig. 5. Validation of the HM-OR-PAM imaging performance. (a) HM-OR-PAM of a red leaf skeleton phantom with a B-scan rate of 420 Hz and 900 Hz. (b) HM-OR-PAM of mouse ear vasculature *in vivo* with a B-scan rate of 420 Hz and 900 Hz.

4. HM-OR-PAM of epinephrine-induced skin vasoconstriction

The high-speed widefield imaging capability of HM-OR-PAM is well suited for studying drug responses in the skin. The mouse ear is a commonly used skin model, which is typically ~10 × 10 mm^2 in dimensions. As a proof of concept, we continuously imaged an entire mouse ear for ~10 minutes, with a volumetric frame rate of 0.125 Hz (or 8 seconds per volumetric imaging). The laser PRR was 600 kHz and the B-scan rate was 420 Hz. One minute after the imaging started, we injected 5 micrograms of epinephrine subcutaneously into the mouse's hind leg. Epinephrine, also known as adrenaline, is commonly used to treat a number of conditions, including anaphylaxis [35], cardiac arrest [36], and superficial bleeding [37]. Epinephrine binds to the alpha receptors of the blood vessels which induces vasoconstriction in the skin. Representative vascular images of the mouse ear at different time points are shown in Fig. 6. Figure 6(a) shows the full-view images of the vasculature network, and Fig. 6(b) shows the close-up images of a small region of interest as indicated by the dashed box in Fig. 6(a). The results clearly show that epinephrine caused substantial vasoconstriction, especially of the microvessels, as indicated by the yellow arrows in Fig. 6(b), resulting in significant reduction in blood perfusion to the ear (see Visualization 2). The PA signal amplitudes decreased due to reduced blood perfusion, reflected by the diminished microvasculature density. The relative changes in the PA signal amplitudes before and post epinephrine injection are shown in Fig. 6(c), which was calculated from the baseline image at 20 sec and the post-injection image obtained at 400 sec. The dynamic and quantitative change over time is shown in Fig. 6(d), revealing the full course of the drug effect. The vasoconstriction effect of epinephrine on the skin microvessels observed by HM-OR-PAM is consistent with the literature reports [38, 39].

Biomedical Optics EXPRESS

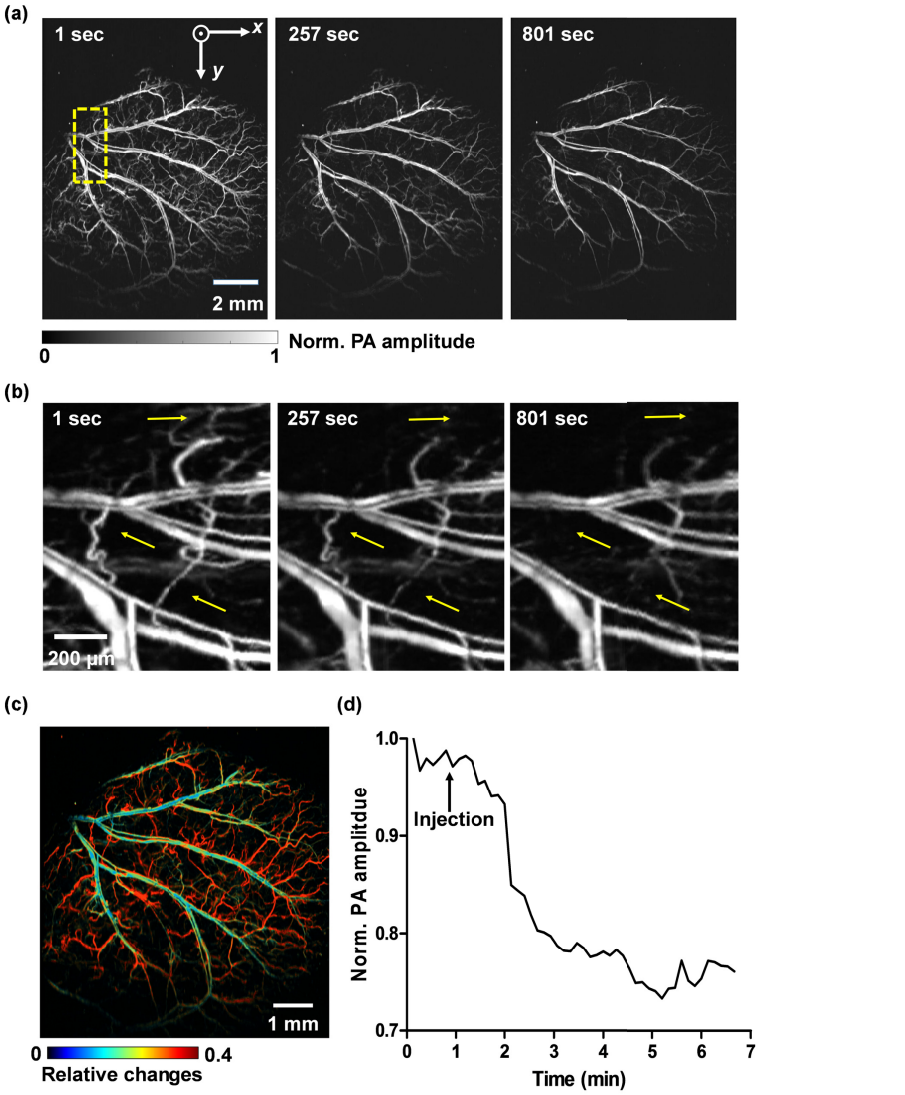

Fig. 6. HM-OR-PAM of the drug responses in a mouse ear. (a) Representative vasculature images of the entire mouse ear at different time points after the epinephrine injection. (b) Close-up images of the region indicated by the dashed box in (a), showing the microvessel constriction (yellow arrows). (c) The relative change in PA signal amplitude before and after epinephrine injection, showing that the smaller vessels experienced stronger drug effect. (d) The time course of average PA signal amplitude over the entire mouse ear before and after the drug injection.

5. HM-OR-PAM of ischemic stroke

HM-OR-PAM has a great potential for mouse brain imaging over the cortex that typically has a size of less than 10 mm in each dimension. Ischemic stroke is a brain vascular disease and an ideal model for HM-OR-PAM. Therefore, ischemic stroke was induced in male C57BL6/j mice (10-12 weeks; 20-25g; Jackson Laboratory, Maine, United States) by middle cerebral artery occlusion (MCAO). The mouse was anesthetized with 1.0-1.5% isoflurane and body temperature of 37 °C was maintained constant throughout the procedure. Transient MCAO surgery was performed as described previously with minor modifications [40]. The left common carotid artery and external carotid artery were isolated and ligated, and the internal

Biomedical Optics EXPRESS

carotid artery was temporarily clipped. Then, a silicon-coated nylon monofilament (Doccol, Sharon, MA, USA) was introduced through a small incision into the common carotid artery and advanced to the bifurcation of anterior cerebral artery and MCA to block blood flow to the MCA territory in the left hemisphere of the mouse brain. The mouse was sacrificed 24 hours after the surgery and brain infarctions were detected by the 2,3,5-triphenyltetrazolium chloride (Sigma Aldrich, St. Louis, United States) staining method (Fig. 7) [41].

Fig. 7. Histological slices of brain infarction after ischemic stroke. The mouse was sacrificed 24 hours after the MCA surgery and brain infarction (white) was detected by the 2,3,5-triphenyltetrazolium chloride staining method.

After 40 minutes of MCAO, blood reperfusion was initiated by withdrawing the monofilament. HM-OR-PAM monitored the whole blood reperfusion process, with a volumetric imaging speed of 0.125 Hz over a 12 × 10 mm^2 region (Fig. 8(a)). The HM-OR-PAM results on the cortical blood flow after ischemic stroke have shown two major observations. Firstly, there was a clear increase in the PA signal amplitudes in vessel-by-vessel mapping of the cortical vasculature after withdrawing the monofilament, reflecting the recovery of the blood perfusion to the originally blocked cortex regions with reduced blood flow (Fig. 8(b)). The blood perfusion recovery is highly heterogenous in space and magnitude (see Visualization 3). The signal increase was mainly concentrated in the left hemisphere, which was consistent with the MCAO procedure. The magnitudes of the signal increase ranged from 20% to 100%, reflecting the fact that different cortical regions experienced various levels of impairment from the MCA blockage [42, 43]. We can also observe that the blood flow in the left hemisphere was not completely blocked by the MCA procedure, mainly because the left hemisphere was supplemented by the right hemisphere via the interconnections/collaterals between two hemispheres [44]. Secondly, there was a heterogenous delay in the starting time of blood reperfusion after the withdrawal of the monofilament. The time course of the blood reperfusion clearly demonstrated that the left middle cortical region, which was closer to the blocked MCA, had a quicker recovery than the left frontal cortical region (Fig. 8(c)). Three representative regions in the left frontal, left middle, and right middle cortex were selected and their signal changes were shown in Fig. 8(d). While the right middle cortex showed no significant changes after the withdrawal of the monofilament, the left middle cortex achieved a total recovery within 4 minutes, and the left front cortex achieved total reperfusion after 11 minutes. A reperfusion delay map of the entire cortex (Fig. 8(e)) highlighted the heterogeneity of the brain hemodynamics after ischemic stroke and truly demonstrated the advantage of HM-OR-PAM as a novel technology capable of high-speed widefield imaging.

Biomedical Optics EXPRESS

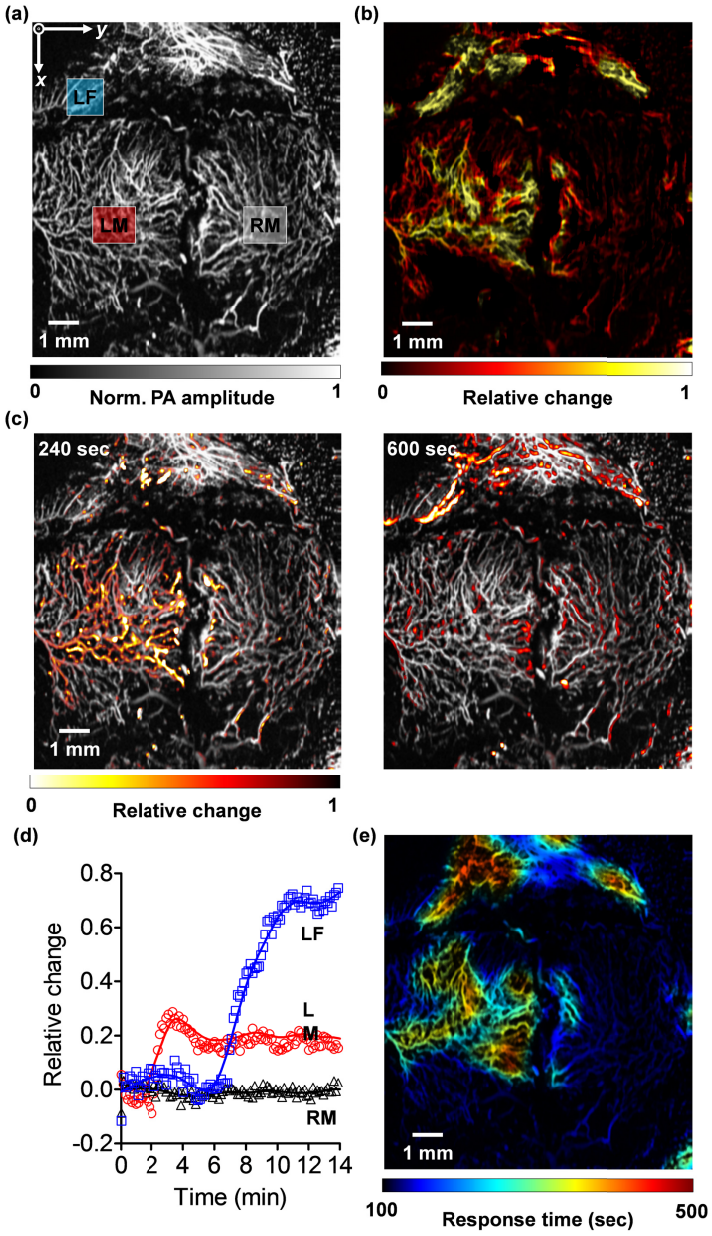

Fig. 8. HM-OR-PAM of vascular reperfusion after ischemic stroke in a mouse brain. (a) The baseline HM-OR-PAM image of the cortical vasculature before the monofilament was inserted into the left MAC. (b) The vessel-by-vessel map of the relative change in the PA signal amplitude 10 minutes after the monofilament withdrawal, showing the blood reperfusion mainly concentrated in the left hemisphere. The PA image at the 60-sec time point was used as the baseline. (c) The relative change in the PA signal amplitude (shown in color) 240 seconds (left) and 600 seconds (right) after the monofilament withdrawal, superimposed on the baseline image (shown in gray). To highlight the different delay time in reperfusion, we used different baselines when changes were quantified. The 240-sec PA image was compared with the 60-sec PA image, and the 600-sec PA image was compared with the 300-sec image. (d) The time courses of the PA signal amplitude change in the selected regions (boxed regions in (a)) in the left front (LF), left middle (LM) and right middle (RM) cortex, showing the heterogenous magnitude and delay in the vascular reperfusion. (e) A vessel-by-vessel map of the reperfusion delay in the entire mouse cortex.

Biomedical Optics EXPRESS

Conclusion and discussion

We have developed a high-speed widefield OR-PAM system, based on a novel water-immersible hexagon-mirror scanner. Driven by a DC motor, the hexagon-mirror scanner has demonstrated fast-rotational scanning with a B-scan rate up to 900 Hz and a consistent scanning range of 12 mm, which have never been achieved by previous photoacoustic microscopy systems. Taking advantage of the high-speed high-resolution widefield imaging capability of HM-OR-PAM, we monitored epinephrine-induced vasoconstriction on the entire mouse ear and vessel reperfusion after ischemic stroke on the entire mouse cortex. The B-scan rate of HM-OR-PAM can be adjusted by controlling the DC-motor driving voltage, providing different scanning step size and imaging speed. The imaging results shown in Fig. 5 have demonstrated that even with a B-scan rate of 900 Hz and an average fast-scanning step size of ~20 μm, HM-OR-PAM can be adjusted by controlling the DC-motor driving voltage, providing different scanning step size and imaging speed. The imaging results shown in Fig. 5 have demonstrated that even with a B-scan rate of 900 Hz and an average fast-scanning step size of ~20 μm, HM-OR-PAM was able to resolve microvessels *in vivo*. By reducing the B-scan rate, HM-OR-PAM can improve its effective spatial resolutions with smaller scanning step sizes, as demonstrated in Figs. 6 and 8.

Nevertheless, there are several limitations in the current HM-OR-PAM system. Firstly, the data acquisition time for each time-resolved A-line signal is approaching the physical limit. With a laser PRR of 600 kHz, each A-line signal acquisition time cannot exceed 1.6 μs to avoid signal overlapping, which corresponds to a maximum depth range of 2.5 mm. Increasing the laser PRR will further reduce the maximally allowed data acquisition time, which may pose a challenge for imaging targets with an uneven surface. This limitation ultimately determines the maximum A-line rate of HM-OR-PAM. Secondly, the revolution rate of the DC-motor limits the maximum B-scan rate. The current DC motor has a maximum speed of 150 revolutions per second with a 5-volt driving voltage, providing a 900-Hz B-scan rate. The B-scan rate can be doubled by using a 12-faced polygon mirror driven by the same DC motor, at the price of halving the scanning range. In this case, the fast-scanning step size can be reduced than that with the hexagon mirror, which can improve the imaging quality. It is also possible to use a more powerful DC motor with a higher revolution speed. However, without fundamentally increasing the laser PRR, a higher B-scan rate would eventually lead to a larger scanning step size and thus a degraded imaging quality.

In conclusion, HM-OR-PAM has overcome the dilemma of imaging speed and field of view in previous OR-PAM systems. The *in vivo* imaging results suggest that HM-OR-PAM can be potentially applied for a wide range of preclinical and clinical research in dermatology, neurology, and cancer biology.

Funding

NIH (NS099590 and NS097554); AHA (18CSA34080277); Duke University MEDx fund.

Acknowledgments

We would like to acknowledge the support of NIH grants NS099590 and NS097554 (to W.Y.), AHA collaborative sciences grant 18CSA34080277 (to W.Y., J.Y., and U.H.), and Duke University MEDx fund (to J.Y.).

Disclosures

The authors declare that there are no conflicts of interest related to this article.

References

1. V. Ntziachristos, J. Ripoll, L. V. Wang, and R. Weissleder, "Looking and listening to light: the evolution of whole-body photonic imaging," Nat. Biotechnol. **23**(3), 313–320 (2005).

Biomedical Optics EXPRESS

2. F. Gao, X. H. Feng, and Y. J. Zheng, "Advanced photoacoustic and thermoacoustic sensing and imaging beyond pulsed absorption contrast," J. Opt. **18**(7), 074006 (2016).
3. K. Maslov, H. F. Zhang, S. Hu, and L. V. Wang, "Optical-resolution photoacoustic microscopy for in vivo imaging of single capillaries," Opt. Lett. **33**(9), 929–931 (2008).
4. L. V. Wang and S. Hu, "Photoacoustic tomography: in vivo imaging from organelles to organs," Science **335**(6075), 1458–1462 (2012).
5. R. Ma, S. Söntges, S. Shoham, V. Ntziachristos, and D. Razansky, "Fast scanning coaxial optoacoustic microscopy," Biomed. Opt. Express **3**(7), 1724–1731 (2012).
6. J. Yao and L. V. Wang, "Sensitivity of photoacoustic microscopy," Photoacoustics **2**(2), 87–101 (2014).
7. G. J. Tserevelakis, D. Soliman, M. Omar, and V. Ntziachristos, "Hybrid multiphoton and optoacoustic microscope," Opt. Lett. **39**(7), 1819–1822 (2014).
8. A. J. Jerri, "Shannon sampling theorem - its various extensions and applications - tutorial review," Proc. IEEE **65**(11), 1565–1596 (1977).
9. J. Laufer, E. Zhang, G. Raivich, and P. Beard, "Three-dimensional noninvasive imaging of the vasculature in the mouse brain using a high resolution photoacoustic scanner," Appl. Opt. **48**(10), D299–D306 (2009).
10. R. L. Shelton, S. P. Mattison, and B. E. Applegate, "Volumetric imaging of erythrocytes using label-free multiphoton photoacoustic microscopy," J. Biophoton. **7**(10), 834–840 (2014).
11. W. Shi, P. Hajireza, P. Shao, A. Forbrich, and R. J. Zemp, "In vivo near-realtime volumetric optical-resolution photoacoustic microscopy using a high-repetition-rate nanosecond fiber-laser," Opt. Express **19**(18), 17143–17150 (2011).
12. E. Z. Zhang, J. G. Laufer, R. B. Pedley, and P. C. Beard, "In vivo high-resolution 3D photoacoustic imaging of superficial vascular anatomy," Phys. Med. Biol. **54**(4), 1035–1046 (2009).
13. N. C. Burton, M. Patel, S. Morscher, W. H. Driessen, J. Claussen, N. Beziere, T. Jetzfellner, A. Taruttis, D. Razansky, B. Bednar, and V. Ntziachristos, "Multispectral opto-acoustic tomography (MSOT) of the brain and glioblastoma characterization," Neuroimage **65**, 522–528 (2013).
14. H. Estrada, J. Turner, M. Kneipp, and D. Razansky, "Real-time optoacoustic brain microscopy with hybrid optical and acoustic resolution," Laser Phys. Lett. **11**(4), 045601 (2014).
15. J. Laufer, E. Zhang, G. Raivich, and P. Beard, "Three-dimensional noninvasive imaging of the vasculature in the mouse brain using a high resolution photoacoustic scanner," Appl. Opt. **48**(10), D299–D306 (2009).
16. R. Ma, A. Taruttis, V. Ntziachristos, and D. Razansky, "Multispectral optoacoustic tomography (MSOT) scanner for whole-body small animal imaging," Opt. Express **17**(24), 21414–21426 (2009).
17. A. Buehler, E. Herzog, D. Razansky, and V. Ntziachristos, "Video rate optoacoustic tomography of mouse kidney perfusion," Opt. Lett. **35**(14), 2475–2477 (2010).
18. H. He, G. Wissmeyer, S. V. Ovsepian, A. Buehler, and V. Ntziachristos, "Hybrid optical and acoustic resolution optoacoustic endoscopy," Opt. Lett. **41**(12), 2708–2710 (2016).
19. H. F. Zhang, K. Maslov, M. Sivaramakrishnan, G. Stoica, and L. H. V. Wang, "Imaging of hemoglobin oxygen saturation variations in single vessels in vivo using photoacoustic microscopy," Appl. Phys. Lett. **90**, 053901 (2007).
20. K. Maslov, H. F. Zhang, S. Hu, and L. V. Wang, "Optical-resolution photoacoustic microscopy for in vivo imaging of single capillaries," Opt. Lett. **33**(9), 929–931 (2008).
21. J. Yao and L. V. Wang, "Photoacoustic microscopy," Laser Photonics Rev. **7**(5), 758–778 (2013).
22. L. Wang, K. Maslov, J. Yao, B. Rao, and L. V. Wang, "Fast voice-coil scanning optical-resolution photoacoustic microscopy," Opt. Lett. **36**(2), 139–141 (2011).
23. J. Y. Kim, C. Lee, K. Park, G. Lim, and C. Kim, "Fast optical-resolution photoacoustic microscopy using a 2-axis water-proofing MEMS scanner," Sci Rep. **5**, 7932 (2015).
24. B. Rao, K. Maslov, A. Danielli, R. Chen, K. K. Shung, Q. Zhou, and L. V. Wang, "Real-time four-dimensional optical-resolution photoacoustic microscopy with Au nanoparticle-assisted subdiffraction-limit resolution," Opt. Lett. **36**(7), 1137–1139 (2011).
25. Z. Xie, S. Jiao, H. F. Zhang, and C. A. Puliafito, "Laser-scanning optical-resolution photoacoustic microscopy," Opt. Lett. **34**(12), 1771–1773 (2009).
26. J. Y. Kim, C. Lee, K. Park, S. Han, and C. Kim, "High-speed and high-SNR photoacoustic microscopy based on a galvanometer mirror in non-conducting liquid," Sci Rep. **6**, 34803 (2016).
27. B. Rao, L. Li, K. Maslov, and L. Wang, "Hybrid-scanning optical-resolution photoacoustic microscopy for in vivo vasculature imaging," Opt. Lett. **35**(10), 1521–1523 (2010).
28. T. Jin, H. Guo, H. Jiang, B. Ke, and L. Xi, "Portable optical resolution photoacoustic microscopy (pORPAM) for human oral imaging," Opt. Lett. **42**(21), 4434–4437 (2017).
29. W. Qin, T. Jin, H. Guo, and L. Xi, "Large-field-of-view optical resolution photoacoustic microscopy," Opt. Express **26**(4), 4271–4278 (2018).
30. J. Yao, L. Wang, J. M. Yang, K. I. Maslov, T. T. W. Wong, L. Li, C. H. Huang, J. Zou, and L. V. Wang, "High-speed label-free functional photoacoustic microscopy of mouse brain in action," Nat. Methods **12**(5), 407–410 (2015).
31. S. Hu, K. Maslov, and L. V. Wang, "Second-generation optical-resolution photoacoustic microscopy with improved sensitivity and speed," Opt. Lett. **36**(7), 1134–1136 (2011).
32. C. Li and L. V. Wang, "Photoacoustic tomography and sensing in biomedicine," Phys. Med. Biol. **54**(19), R59–R97 (2009).

Biomedical Optics EXPRESS

33. A. Colantuoni, S. Bertuglia, and M. Intaglietta, "Variations of Rhythmic Diameter Changes at the Arterial Microvascular Bifurcations," Pflugers Arch. **403**(3), 289–295 (1985).
34. J. Yao, C. H. Huang, L. Wang, J. M. Yang, L. Gao, K. I. Maslov, J. Zou, and L. V. Wang, "Wide-field fast-scanning photoacoustic microscopy based on a water-immersible MEMS scanning mirror," J. Biomed. Opt. **17**(8), 080505 (2012).
35. S. F. Kemp, R. F. Lockey, and F. E. Simons; World Allergy Organization ad hoc Committee on Epinephrine in Anaphylaxis, "Epinephrine: the drug of choice for anaphylaxis-a statement of the world allergy organization," World Allergy Organ. J. **1**(7), S18–S26 (2008).
36. A. Lundin, T. Djärv, J. Engdahl, J. Hollenberg, P. Nordberg, A. Ravn-Fischer, M. Ringh, S. Rysz, L. Svensson, J. Herlitz, and P. Lundgren, "Drug therapy in cardiac arrest: a review of the literature," Eur. Heart J. Cardiovasc. Pharmacother. **2**(1), 54–75 (2016).
37. M. Shoroghi, S. H. Sadrolsadat, M. Razzaghi, F. Farahbakhsh, M. Sheikhvatan, M. Sheikhfathollahi, and A. Abbasi, "Effect of different epinephrine concentrations on local bleeding and hemodynamics during dermatologic surgery," Acta Dermatovenerol. Croat. **16**(4), 209–214 (2008).
38. J. S. Floras, P. E. Aylward, R. G. Victor, A. L. Mark, and F. M. Abboud, "Epinephrine facilitates neurogenic vasoconstriction in humans," J. Clin. Invest. **81**(4), 1265–1274 (1988).
39. A. C. Yard and P. J. Kadowitz, "Studies on the mechanism of hydrocortisone potentiation of vasoconstrictor responses to epinephrine in the anesthetized animal," Eur. J. Pharmacol. **20**(1), 1–9 (1972).
40. Y. C. Wang, E. H. Sanchez-Mendoza, T. R. Doeppner, and D. M. Hermann, "Post-acute delivery of memantine promotes post-ischemic neurological recovery, peri-infarct tissue remodeling, and contralesional brain plasticity," J. Cereb. Blood Flow Metab. **37**(3), 980–993 (2017).
41. M. Jiang, S. Yu, Z. Yu, H. Sheng, Y. Li, S. Liu, D. S. Warner, W. Paschen, and W. Yang, "XBP1 (X-Box-Binding Protein-1)-Dependent O-GlcNAcylation Is Neuroprotective in Ischemic Stroke in Young Mice and Its Impairment in Aged Mice Is Rescued by Thiamet-G," Stroke **48**(6), 1646–1654 (2017).
42. O. Baranova, L. F. Miranda, P. Pichiule, I. Dragatsis, R. S. Johnson, and J. C. Chavez, "Neuron-specific inactivation of the hypoxia inducible factor 1 alpha increases brain injury in a mouse model of transient focal cerebral ischemia," J. Neurosci. **27**(23), 6320–6332 (2007).
43. D. Knowland, A. Arac, K. J. Sekiguchi, M. Hsu, S. E. Lutz, J. Perrino, G. K. Steinberg, B. A. Barres, A. Nimmerjahn, and D. Agalliu, "Stepwise recruitment of transcellular and paracellular pathways underlies blood-brain barrier breakdown in stroke," Neuron **82**(3), 603–617 (2014).
44. J. M. Beis, C. Keller, N. Morin, P. Bartolomeo, T. Bernati, S. Chokron, M. Leclercq, A. Louis-Dreyfus, F. Marchal, Y. Martin, D. Perennou, P. Pradat-Diehl, C. Prairial, G. Rode, M. Rousseaux, C. Samuel, E. Sieroff, L. Wiart, and P. Azouvi; French Collaborative Study Group on Assessment of Unilateral Neglect (GEREN/GRECO), "Right spatial neglect after left hemisphere stroke: qualitative and quantitative study," Neurology **63**(9), 1600–1605 (2004).